# NAVIER-STOKES AND COMPREHENSIVE ANALYSIS PERFORMANCE PREDICTIONS OF THE NREL PHASE VI EXPERIMENT

**Earl P.N. Duque**[*]
Northern Arizona University
Dept. of Mechanical Engineering
Flagstaff, Arizona

**Michael D. Burklund**[**]
Northern Arizona University
Dept. of Mechanical Engineering
Flagstaff, Arizona

**Wayne Johnson** [#]
Army/NASA Rotorcraft Division
NASA Ames Research Center
Moffett Field, California

## Abstract

A vortex lattice code, CAMRAD II, and a Reynolds-Averaged Navier-Stoke code, OVERFLOW-D2, were used to predict the aerodynamic performance of a two-bladed horizontal axis wind turbine. All computations were compared with experimental data that was collected at the NASA Ames Research Center 80- by 120-Foot Wind Tunnel. Computations were performed for both axial as well as yawed operating conditions. Various stall delay models and dynamics stall models were used by the CAMRAD II code. Comparisons between the experimental data and computed aerodynamic loads show that the OVERFLOW-D2 code can accurately predict the power and spanwise loading of a wind turbine rotor.

## Introduction

The design process of a wind turbine blade requires accurate, reliable and robust numerical predictions of wind turbine rotor performance for the machine's full range of operating conditions. The literature reports various methods that compare numerical predictions to experiments. The methods vary from Blade Element Momentum Theory (BEM) ( Refs. 1, 2 ), Vortex Lattice (VL) (Refs. 3), to variants of Reynolds-averaged Navier-Stokes (RaNS) (Refs. 4, 5) The BEM and VL methods consistently show discrepancies in predicting rotor power at higher wind speeds mainly due to inadequacies with inboard stall and stall delay models. The RaNS methodologies show promise in predicting blade stall. However, many speculate that inaccurate rotor vortex wake convection, boundary layer turbulence modeling and grid resolution have limited their accuracy. In addition, the inherently unsteady stalled flow conditions become computationally expensive for even well equipped research labs.

The National Renewable Energy Laboratory (NREL), recently completed an experimental program known as the NREL Unsteady Aerodynamics Experiment Phase VI.( Ref. 6 ) In this experiment, they tested a two-bladed twisted and tapered 10-meter diameter wind turbine in the NASA Ames Research Center 80- by 120-Foot Wind Tunnel. This program recorded performance and loads data over an extensive matrix of operating conditions. A blind numerical study that involved 20 different participants who used various types of prediction codes showed a disturbing range of prediction capabilities. These results demonstrated that there still remains a lack of understanding in the aerodynamic behavior of wind turbine blades. (Ref. 7)

The work presented in this paper will show comparisons between two rotor performance prediction computer codes – OVERFLOW-D2 and CAMRAD II. OVERFLOW-D2 is a Reynolds-Averaged Navier-Stokes code developed by Bob Meakin at NASA Ames Research Center. CAMRAD II, developed by Wayne Johnson, was originally developed as a comprehensive vehicle dynamics and aerodynamics code for the rotorcraft industry and has been modified to model horizontal axis wind turbines. It utilizes a vortex lattice with free wake (FW) model.

---

[*] Associate Professor, Senior Member AIAA
[**] Undergraduate Research Assistant
[#] Research Scientist, Member AIAA
Presented at 22nd ASME Wind Energy Symposium, Reno NV, Jan 2003

Both methodologies were applied to the Phase VI rotor in an upwind configuration, for both axial wind conditions as well as at fixed yaw error. To date, only the CAMRAD II results have been analyzed for yawed flow conditions. In addition, various stall delay and dynamic stall delay models were investigated. The results presented here demonstrate a significant capability in predicting the aerodynamic loads and power generated by solving from first principles the flow around a wind turbine. In addition, these results yield some further insight into the mechanism of blade stall delay and dynamic stall.

## Methodology

CAMRAD II (Refs.8) is a vortex lattice code. It was originally developed as a comprehensive vehicle dynamics and aerodynamics code for the rotorcraft industry and has been modified to model horizontal axis wind turbines (HAWT). It utilizes a vortex lattice with free wake (FW) model. In addition, the CAMRAD II code has the capability to run in BEM mode. It also has the capability to simulate the dynamic response of the turbine's flapping or teetering motions and nacelle yaw.

Like most vortex lattice and BEM methods, CAMRAD II requires two-dimensional airfoil lift and drag data for the predictions. The airfoil of interest for this study is the 21-percent thick S809; an airfoil from the NREL thick-airfoil family for HAWT applications (Ref. 9). For this purpose the airfoil was designed to have a sustained maximum lift, minimal sensitivity of lift to roughness, and low profile drag. An extensive experimental database for use in BEM methods was developed at OSU (Ref. 9).

Airfoil tables were also generated via the MSES code. The MSES multi-element airfoil code (Refs. 10 and 11) represents an extension of the single-element ISES compressible flow airfoil code. In this method, the streamline-based Euler equations and boundary-layer equations are solved simultaneously using a full-Newton method. The boundary layers and wakes are described with a two-equation lagged dissipation integral boundary layer formulation and an envelope $e^N$ transition criterion. The initial streamline grid is generated through the solution of a panel method at a specified angle of attack and then modified after each Newton iteration as part of the solution. Displacement bodies based on the shear-layer displacement thickness are used to modify the element surface geometry and are incorporated into the solution after each iteration. This strong inviscid/viscous coupling enables MSES to predict the effects of laminar separation bubbles and other regions of limited flow separation on the pressure distribution.

Two types of airfoil tables were used with CAMRAD II. The first uses the S809 experimental airfoil data obtained from Ref. 9. That data consists of $C_l$ and $C_d$ for angles-of-attack from $-2.23^o$ to $89.9^o$ and constructed by NREL from the OSU data. This table was extended to cover a complete angle of attack range of $\pm 180^o$.

The second airfoil table uses the MSES code to provide sectional lift and drag coefficients ($C_l$ and $C_d$) for several Reynolds numbers. However, since MSES only predicts aerodynamic coefficients up to maximum $C_l$, the S809 experimental data were used beyond stall. Figure 1 illustrates the resulting lift polars used by CAMRAD II.

To obtain accurate rotor sectional lift characteristics and hence accurate power prediction, the two-dimensional airfoil data needs to be corrected for inboard stall delay effects. As summarized by Snel and van Holten (Ref. 12), Corrigan and Schillings (Ref. 13), and Du and Selig (Ref. 14) the sectional maximum lift coefficient will exceed the two-dimensional airfoil maximum lift for the inboard sections of a rotor. Corrigan and Schillings developed their stall delay model based upon observations of experimentally measured stall delay on rotors. They applied this model to their helicopter rotor performance code and were able to accurately predict rotor power. Snel and van Holten performed an order of magnitude analysis on the 3-Dimensional boundary layer equations. They show that when the flow begins to separate that the Coriolis force has a significant impact on the spanwise momentum in the boundary layer.

Du and Selig (Ref. 14) developed a stall delay model designed for use in BEM and VL methods. This model is based upon the analysis of 3-D integral boundary layer equations to determine the effects of rotation on boundary layer separation.

The second numerical method used in this study is a Reynolds-averaged Navier –Stokes code known as OVERFLOW-D2. Buning, et.al, first developed the OVERFLOW code. (Ref. 15). Since then, various versions of OVERFLOW have been developed and applied to both rotorcraft (Refs.16, 17) as well as a HAWT (Refs. 18).

In the present work, the OVERFLOW-D2 version 1.5d was applied to the Phase VI rotor. (Ref. 19) Like other versions of OVERFLOW, this version solves the compressible form of the Reynolds Averaged Navier-Stokes equations using an implicit finite difference approach with overset grids. The method is first order

accurate in time with 4th order central differences for spatial differences. 2nd and 4th order central difference dissipation terms are added for stability.

One major difference of this version is that it utilizes overset uniform Cartesian meshes for the background farfield meshes. This approach results in a set of near-body curvilinear meshes that overset onto a uniform farfield mesh. Figure 2a, illustrates a cut through the grid system, showing the uniform Cartesian meshes.

The OVERFLOW-D2 code generates this system of overset uniform Cartesian grids. The grids start with a user specified grid spacing of 0.05. The code then builds multiple layers of overset Cartesian grids. Each subsequent layer coarsens by a factor of two. The system for the current rotor computation consists of five layers of grid coarsening that extends approximately two rotor diameters above and below the rotor hub center. This system consists of 82 individual overset grids forming a total of 11,486,000 grid points.

The near body curvilinear grid system consists of 12 grids to fully describe two blades and a simplified hub attachment. The near body grids were generated using Chan's hyperbolic grid generation technique known as HYPGEN and OVERGRID (Ref. 20). Each grid extends approximately one chord length from the rotor body surface. The initial normal grid spacing is approximately $5.0e^{-05}$ of reference chord. This spacing corresponds to $y^+$ approximately equal to 5.0. The grid stretches using a tangent function such that the end spacing is approximately 0.05 of the reference chord. The near body grids total 1,574,000 points. Figure 2b and c illustrate the rotor's surface grid near the tip region and the curvilinear mesh for the main parts of the rotor.

OVERFLOW-D2 has several options for modeling boundary layer turbulence. One method is an algebraic turbulence model known as Baldwin- Lomax.(Ref. 21). In addition it has a 1-equation model by Baldwin and Barth (Ref. 22). The Baldwin-Barth model was used for all the calculations. In addition, the rotor boundary layer was assumed to be fully turbulent.

The OVERFLOW-D2 computations were performed on the Renewable Energy Computational Fluid Dynamics Laboratory Compute Cluster located at the College of Engineering and Technology at Northern Arizona University. The compute cluster consists of twenty-four rack mounted machines and 3 desktop systems. Sixteen of the rack mounts are custom built systems consisting of 1.4Ghz AMD processors, 512MB of DDRAM, 60GB ATA hard drives, and dual 100Based-T Network Interface Cards (NIC). The remaining 8 rack-mounted machines are commercially available servers. Each machine has two AMD1.8 Ghz processors, 80GB ATA disk storage and 1GB of DDRAM memory. The 3 desktop systems are Dell 420 workstations. Each machine has two 800Mhz Pentium III processors, 1GB of RDRAM, 40 GB of SCSI hard drive, high-end video graphics and dual 100Based-T NICs. All the systems utilize a dedicated switched 100Based-T private network. The Dell machines serve both as compute nodes as well as graphical workstations. The remaining servers work only as compute nodes. All machines use the Linux operating system Red Hat version 7.3. (Ref. 23 ) and the Portland Group Cluster Development Toolkit for code compilation.

The code makes use of these compute nodes by using distributed parallel computing techniques. The code automatically takes the system of overset grids and divides them up into groups of grids. The numbers of groups are consistent with the number of available compute processors. Each group is placed onto a separate processor and boundary information is passed between the compute nodes with each time step. This method is very efficient, scalable and well load balanced making for lower turn around time for a given computation.

All OVERFLOW-D2 computations were computed in inertial coordinates. For axial flows, source terms were used to capture the rotating flow with a static grid. A typical converged axial flow computation required approximately 5000 times steps totaling 25.8 hours of wall clock time on 8 processors. Yawed flows utilized moving grids whereby the 12 near-body grids move through the Cartesian grids. Each revolution of the rotor required 7200 time steps and 48.5 hours of wall clock time on 8 processors.

## Results and Discussions

Axial Cases

Figure 3 compares the aerodynamic power predicted by the two methods, and the experimentally measured power. The dashed lines represents results from the CAMRAD II code using various stall delay models. The diamond symbols are the NREL experimental data. The solid line represents data from OVERFLOW-D2 code.

The OVERFLOW-D2 results match the measured power quite well, including at high wind speeds where the blades are operating in stalled flow. The CAMRAD II results illustrate the need for a stall delay model. This requirement becomes evident at a wind speed of 10m/s. With the stall delay model, the CAMRAD II code slightly overpredicts the power at the wind speeds up to 15 m/s. Above that wind speed, the code grossly overpredicts the power.

The spanwise loading distributions show the source of the power prediction discrepancies. Figure 4 compares the measured and calculated normal force coefficient. The experimental and OVERFLOW-D2 forces result from an integration of the chordwise pressures only. The experimental data are limited to the spanwise station locations of r/R= 30%, 47%, 63%, 80 % and 95%. The OVERFLOW-D2results were obtained by using the FIELDVIEW flow visualization software to perform integrations of the blade surface pressures.

Each method uses a slightly different reference dynamic pressure, Q. The experiment uses a measured total pressure that was obtained from pitot tubes located at the various radial stations. The CAMRAD II code calculates the dynamic pressure from $1/2\rho V^2_{ref}$ with the resultant velocity, $V_{ref}$, computed from the oncoming wind speed, the local rotational velocity, plus the local computed inflow. The OVERFLOW-D2 code utilizes the oncoming wind speed and the local rotation velocity.

Figure 4 shows the normal force coefficient distribution at each of the six wind speeds, 7, 10 , 13, 15, 20 and 25 m/s. The solid blue line represents the OVERFLOW-D2 results while the dashed red line represents the CAMRAD II results. For all the wind speeds, OVERFLOW-D2 does a much better job of obtaining not only the correct trend in the normal force, but also the correct absolute magnitude within the experimental uncertainty.

At 7 m/s, the CAMRADII and OVERFLOW-D2 code have very similar trends. However, as is expected from the power plot, the OVERFLOW-D2 loading under predicts the normal force. At 10 m/s, the codes still have somewhat similar trends, however at midspan and at the very tip, the codes deviate from one another. At mid span, CAMRAD II matches the data whereas the OVERFLOW-D2 code slightly underpredicts. At the tip, where the loading has a big effect on the rotor torque and hence power, the CAMRAD results slightly overpredict while the OVERFLOW-D2 results match the data.

At 13 m/s, the blade has partially stalled. Both methodologies miss the spanwise loading distributions. They both have similar trends however. The CAMRAD II code does better in capturing the inboard stall delay, where $C_n$ exceeds 2.0 at r/R=30%, but then overloads near the tip. The OVERFLOW-D2 code exhibits a better trend, but then under predicts the loading consistently along the blade span. At 15m/s the blade continues to stall as evidenced by values of $C_n$ = 1.0 at the 47% and 63% radial stations. Along the mid span, the $C_n$ has plateaued with the local sections stalled and exhibiting some stall delay effect. The OVERFLOW-D2 code shows a trend somewhat like the experiment, however, it fails to pick up the stall delay at 63%. In contrast, the CAMRAD code overpredicts the stall delay at 47% radius, but then matches at 63%.

For the fully stalled cases, 20m/s and 25 m/s, the OVERFLOW-D2 matches the experimental data within the experimental uncertainty along all radial locations. The CAMRAD II code consistently overpredicts the spanwise loading for these fully stalled flow conditions. This behavior is a direct result of the stall delay model.

The normal force coefficient gives a picture of how well each method predicts the sectional stall effects. However, it does not give a good picture of the actual contribution to the rotor torque and power because the local dynamic pressure decreases with radius. Figure 5 circumvents this issue by scaling the local normal force coefficient by the local dynamic pressure. At 7 and 10 m/s, the scaled normal forces for the two methods are very similar with differences primarily at the very root and at the very tip. At the very tip where the loads make the greatest contribution to the power, the CAMRAD II code consistently overpredicts the loading.

At 13 m/s, the CAMRAD II code captures the loading at the tip much better than the OVERFLOW-D2 code, although, both methods show the same trend. At 15 m/s, the methods show very different trends and magnitudes. As in the normal force coefficient distributions for this wind speed, the codes have opposing trends at the 47% and 63% radial stations. Finally, for the stalled cases at 20 and 25m/s, the OVERFLOW-D2 matches trends and magnitude along the entire rotor span.

Figure 6 though Figure 11 compares the surface pressure coefficient distribution predicted by the OVERFLOW-D2 code to the experimental data. As expected from the spanwise and integrated power computations, the surface pressures compare very well against the experimental data. For most of the spanwise stations, the predicted surface pressures lie very close to the experimental data. However, some discrepancies exist.

All the pressure plots show a pressure oscillation at the trailing edge. This oscillation is more pronounced at the inboard radial locations in comparison to the outer radial stations. This anomaly can be attributed to the compressible formulation of the code compared to the incompressible nature of the wind turbine flow particularly along the inboard stations.

The pressure plots give further insight into the differences in predicted and measured local flow that is not shown in the radial distributions or integrated power. In particular, the pressure distribution at r/R=47% in Figure 7 shows a significant difference in the leading edge pressure distribution while Figure 4 shows a force coefficient predicted within experimental uncertainty. The computed pressure distribution has more loading towards the local cross section leading edge as compared to the experiment. Beyond approximately 20% chord the experiment shows more loading than the computed. For this section, the experiment and computation may result in the same integrated force yet have very different pressure distributions.

At 13m/s , Figure 8, the difference in the leading edge pressure distribution moves outboard to r/R = 63%. In addition, we see pressure distribution differences at r/R =30% becoming more pronounced. Up to an r/R = 63% the computations tend to predict a higher leading edge suction peak where as the experimental leading edge pressures have a flatter distribution. Along the outer radial sections, the correlation between experiment and computations recovers.

Along the inboard sections, the local flow has started to stall resulting in local pockets of separated flow. This flow is inherently unsteady. The current computations were all performed using steady state techniques. Therefore, the unsteady time-averaged behavior captured by the experiment may not correlate well with the current computations. The OVERFLOW-D2 code is capable of unsteady flow predictions; future studies are needed to completely study the unsteady nature of the stalled flows.

At 20 and 25 m/s, Figure 10 and Figure 11 show a predominately flat pressure distribution on the blades upper surface indicating fully stalled conditions. Figure 10 shows that at 20/ms, the leading edge suction peak behavior predicted at 13 and 15 m/s has gone away and that the OVERFLOW-D2 code predicts the distribution rather well. However, at r/R=30% the comparisons do not agree; the aft part of the airfoil distributions do not agree. Again, this discrepancy exists because of the unsteadiness in the flow not well captured.

The series of flow visualization images shown in Figure 12 illustrate the onset of the stalled flow that was indicated by the surface pressure and radial normal force distributions. The images show velocity contours along a cut plane through the computational domain for one of the rotor blades. The views are made of one of the rotor blades with the blade pointing up and nearly orthogonal to the blade leading edge. The wind flows from left to right resulting in a view into the blade's leading edge. The normalized velocity magnitude contours shown vary from 0.0 to 0.10.

At 7 and 10 m/s, the contours illustrate the predominately attached flow and some of the detail in the wake down stream. At 13 and 15 m/s, the inboard sections begin to separate as indicated by the contours to the right of the rotor blade (upper surface). With increasing wind speed, the separation region grows. At 25 m/s, the separated region spreads across the complete radius blade.

As blade stall occurs, spanwise flow in the boundary layer becomes more prevalent. Flow visualizations in Figure 13 through Figure 15 illustrates the development of this flow by displaying sectional cuts of velocity magnitudes at r/R = 47% and 80%. In addition, velocity vectors are rendered at the 3$^{rd}$ grid point off the surface. This grid point is on the average within $y^+ = 10$ in the boundary layer. The velocities in these figures are taken in non-inertial space.

Figure 13 presents the visualizations at 7 m/s. The flow is fully attached as presented earlier. The velocity contours show the development of the boundary layer and the significant boundary layer growth past the airfoil maximum thickness. The velocity vectors further show the predominately attached flow. Some spanwise flow exists in the hub shank and in the inner most tapered region.

Figure 14 shows the partially separated flow that exists at 13 m/s. At the inboard section, the velocity contour shows a leading edge boundary layer separation. At the outer radial section, the boundary layer separates at the maximum thickness location. The velocity vectors show that the separated flow results in a spanwise flow within the boundary layer. Along the inboard sections, the velocity vectors all tend to show a radial flow. At approximately r/R=50% the velocity vectors first show attached flows indicated by the vectors pointing towards the trailing edge. Upon separation, the velocity vectors turn toward the blade tip indicating flow separation and spanwise flow.

When the rotor fully stalls, the OVERFLOW-D2 results indicate spanwise flow along the entire blade span as shown in Figure 15. Both velocity contours demonstrate flows with leading edge boundary layer separation. The velocity vectors all point towards the blade tip. In addition, a chordwise flow towards the leading edge increases with radius.

Yawed Cases

Experimental data at yaw errors of 10, 30 and 60 degrees and wind speeds of 10, 13 and 15 m/s were investigated. To date, only data from CAMRAD II have been post-processed. For all these cases, significant regions of stall delay exist, much as in the axial flow cases. In addition, with the extreme yaw cases and higher wind speed, dynamic stall events are expected to occur. Therefore, both a stall delay model as well as a dynamic stall model is required.

Figure 16 presents the normal force coefficient and illustrates the need for a stall delay model. The figures present the r/R=30% forces at the 10m/s wind speed with 10 degrees of yaw error. Consistently at each azimuth angle, the loading is underpredicted if the stall delay model is not used. With the stall delay model, the method shows better correlation.

Figure 17 illustrates the azimuthal variation of the normal force coefficient at three radial locations, 30%, 63% and 95% for a wind speed of 10 m/s and rotor yaw error of $10^o$. In addition, the plots compare CAMRAD II computations that use only the Du-Selig stall delay model (Case02), and computations that use the Du-Selig stall delay model along with the Leishman-Beddoes dynamic stall model (Case 11). The normal force coefficients show little difference between the two methodologies for this yaw error condition.

Figure 18 illustrates the normal force coefficient variation also at 10 m/s but at an increased yaw error of $30^o$. At this operating condition, we see significant differences between the two methods, particularly for the inner most radial station of 30%. The dynamic stall model tends to cause significant overprediction of the loads particularly in the forth quadrant ( $270^o$ – $360^o$). Figure 19 illustrates that at $60^o$ of yaw error, the discrepancy between experimental data and predicted becomes even more pronounced in the first ($0^o$-$90^o$) and forth quadrant. The dynamic stall model has a significant problem as yaw and unsteady effects become more pronounced.

## Conclusions

This paper presented a comparison of the performance predictions of the NREL Phase VI rotor using OVERFLOW-D2 and the CAMRAD II code. The results show that the OVERFLOW-D2 code can predict the stalled rotor performance in axial flow. The CAMRAD II code does a good job at predicting the non-stalled rotor performance. At higher wind speeds, even with the stall delay model, the method fails to capture the stalled rotor performance. The OVEFLOW-D2 results show significant spanwise flow upon onset of stall. Future stall delay models need to capture this flow phenomena in order to provide consistently accurate results.

## Acknowledgements

Portions of this work was sponsored by:

1. The State of Arizona's Technology and Research Initiative Fund
2. Northern Arizona University's Center for Sustainable Environments
3. Northern Arizona University/NASA Space Grant Office
4. National Renewable Energy Laboratory/Dept. of Energy Subcontract DCX-7-17211-01 entitled Army/NASA CFD Project.

The authors would also like to acknowledge the assistance of Dr. Niels Sorrensen of Riso National Laboratory in Denmark for kindly providing his surface grid of the Phase 6 rotor and for many useful discussions.

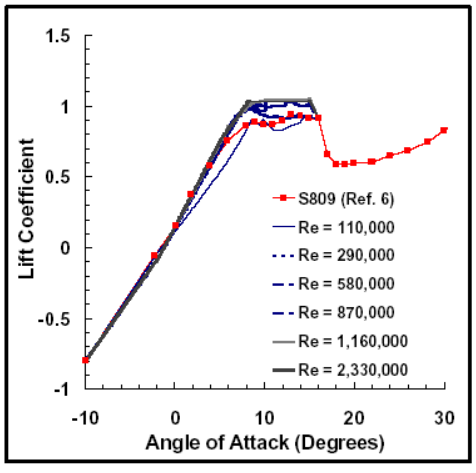


**Figure 1 - Lift polar from NREL data and MSES**

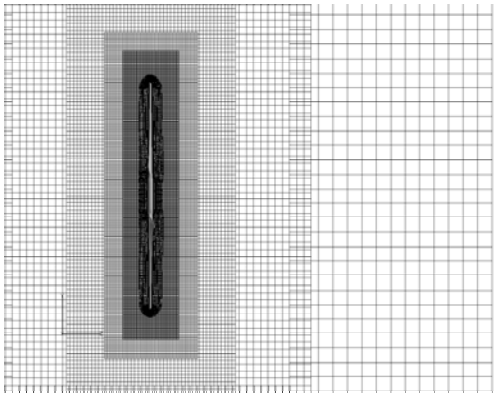

a) Cut plane through overset grid system

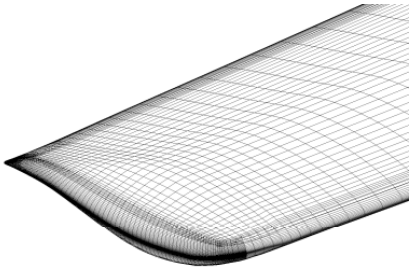

b) Surface grid details

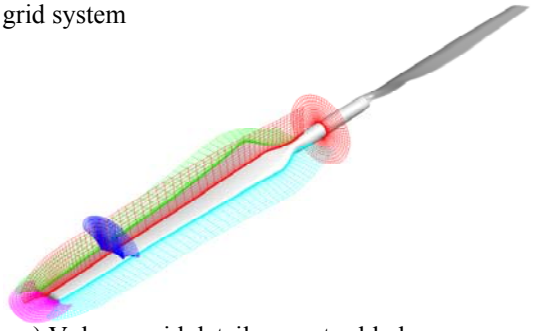

c) Volume grid details on rotor blade

**Figure 2 – Phase 6 Grid Details**

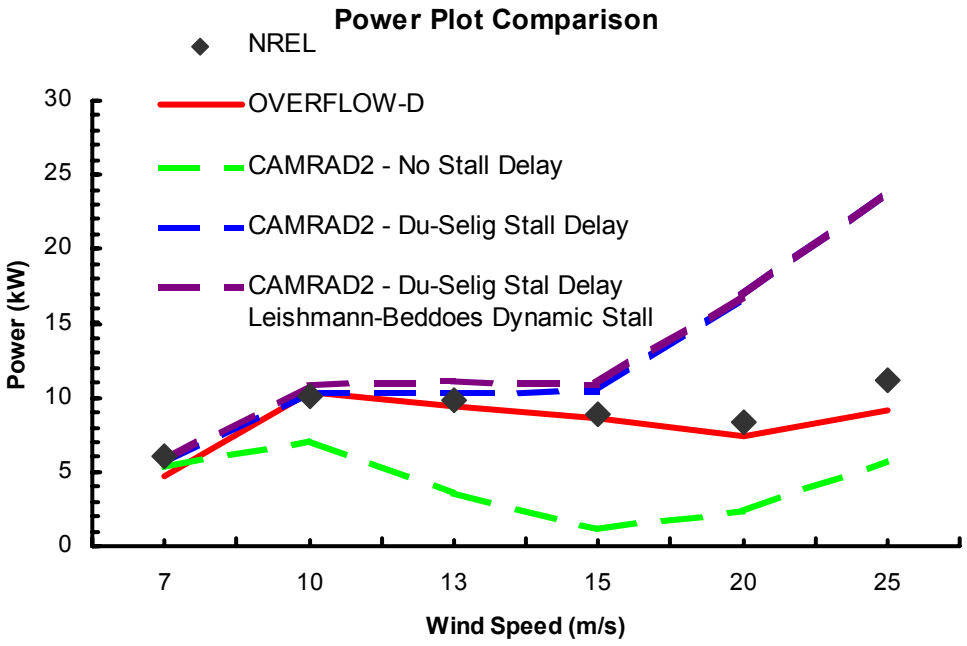


**Figure 3 - Comparison of Predicted and Measured Aerodynamic Power Phase VI Rotor, Upwind, $0^o$ Yaw Error**

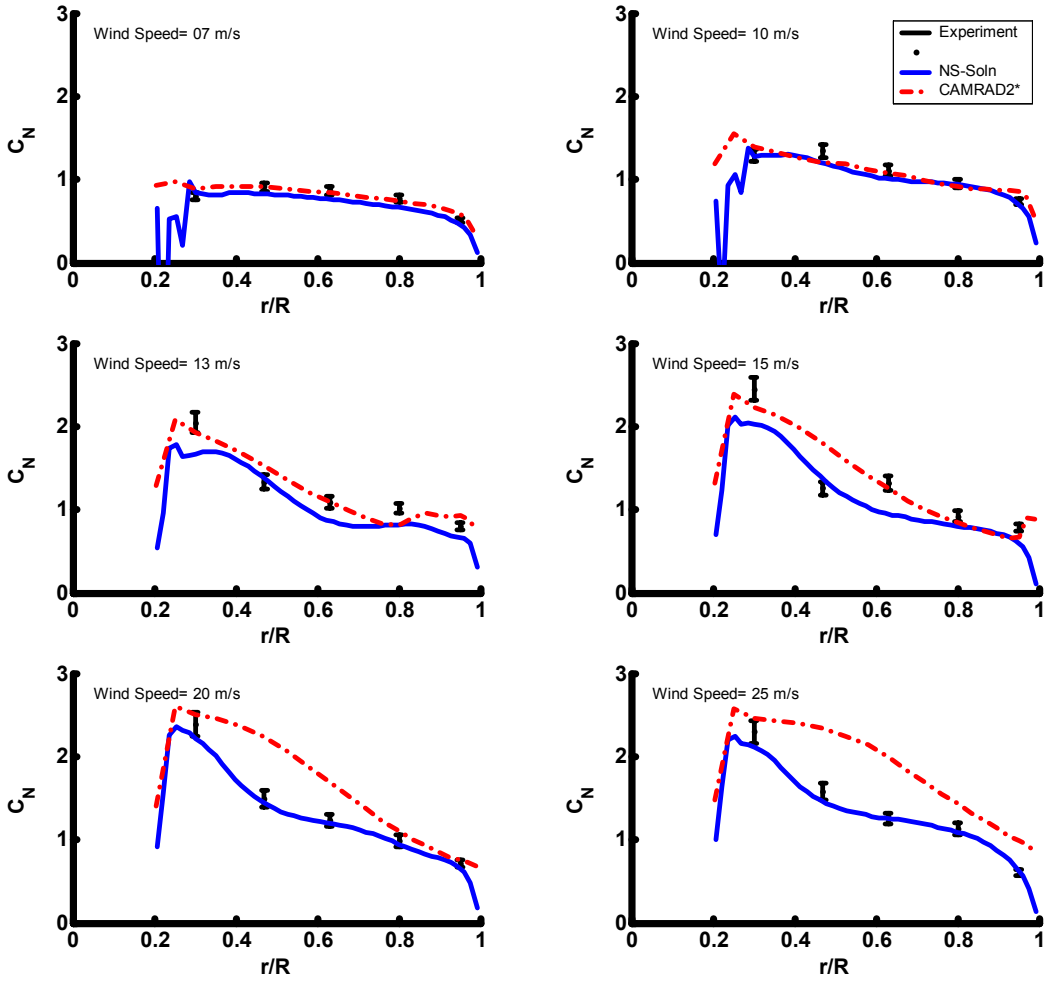


**Figure 4 Radial Normal Force Coefficient**

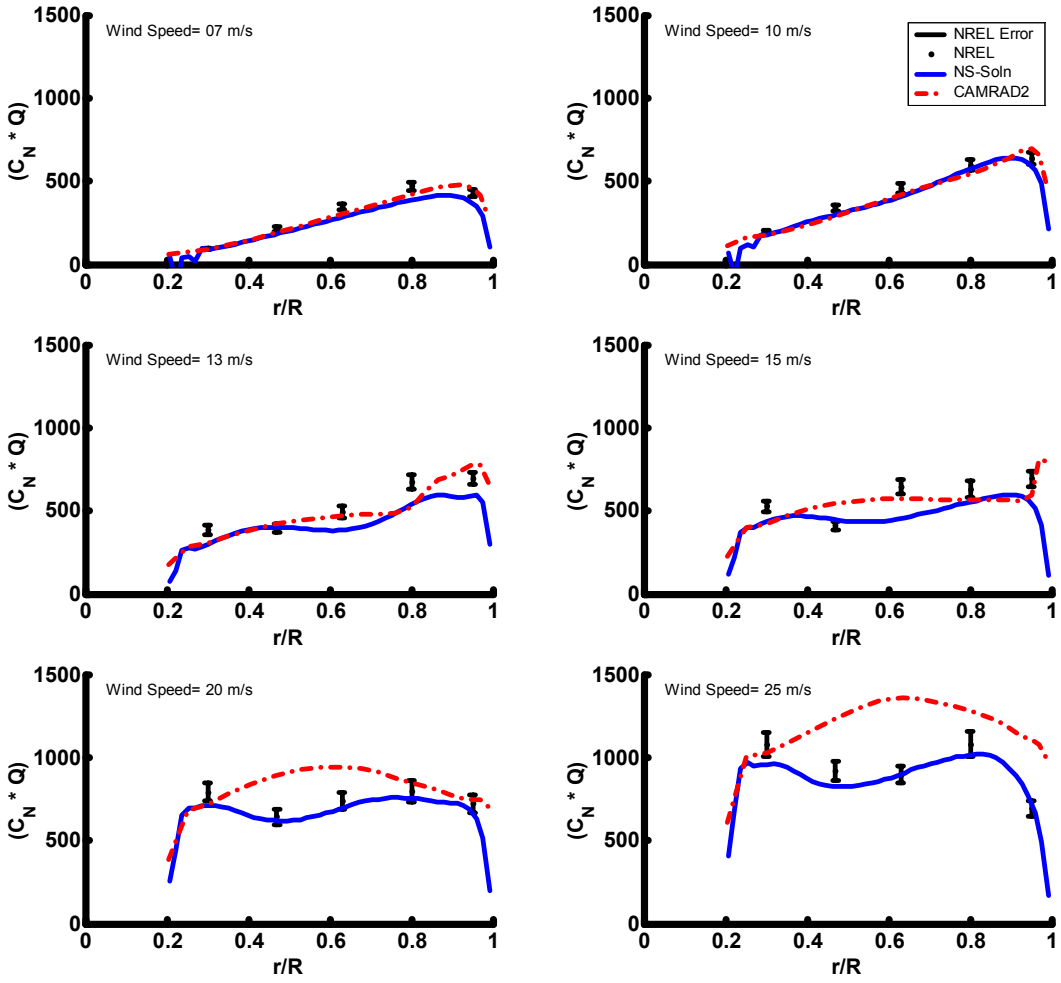


**Figure 5 Radial Normal Force Coefficient Scaled by Local Dynamic Presure (Q)**

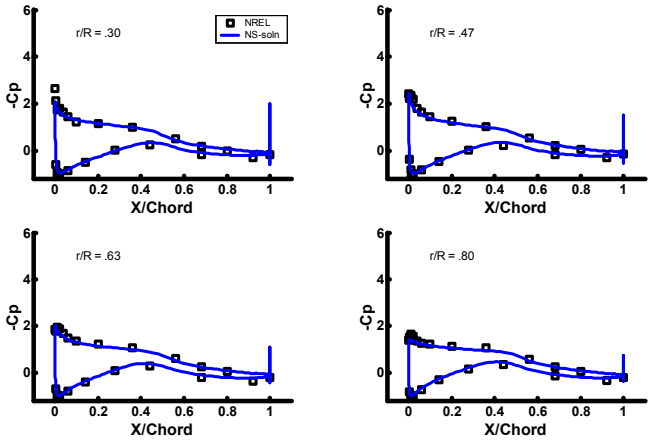


**Figure 6 - Pressure Coefficient, 7 m/s**

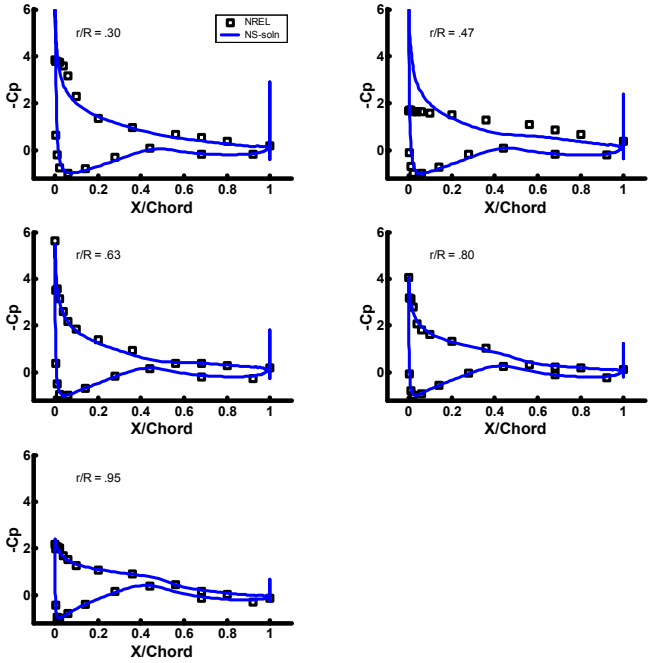


**Figure 7 - Pressure Coefficient, 10m/s**

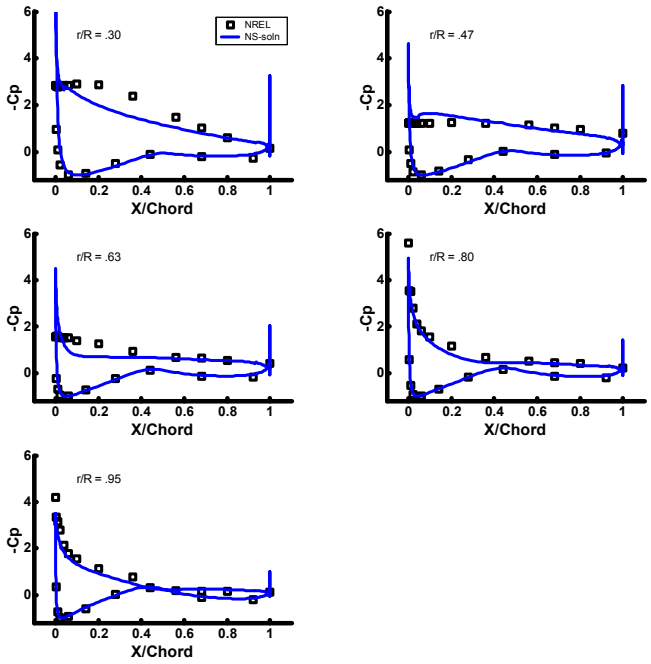


**Figure 8 - Pressure Coefficient, 13 m/s**

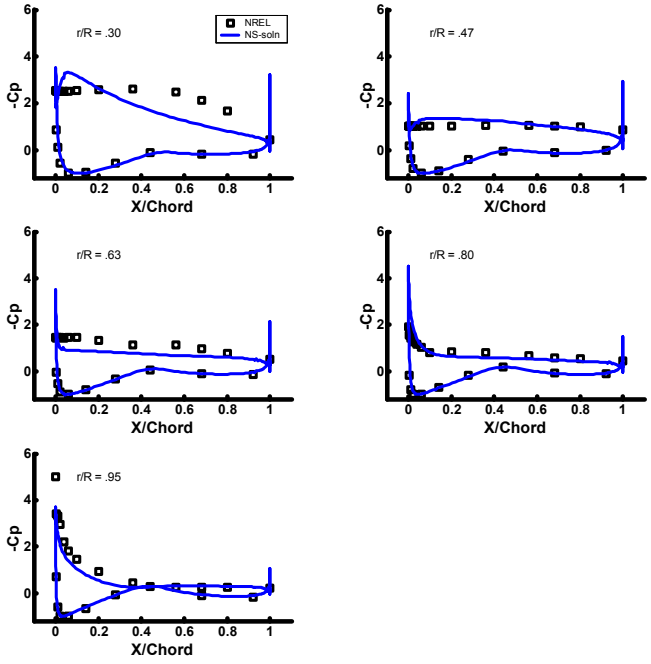


**Figure 9 - Pressure Coefficent, 15 m/s**

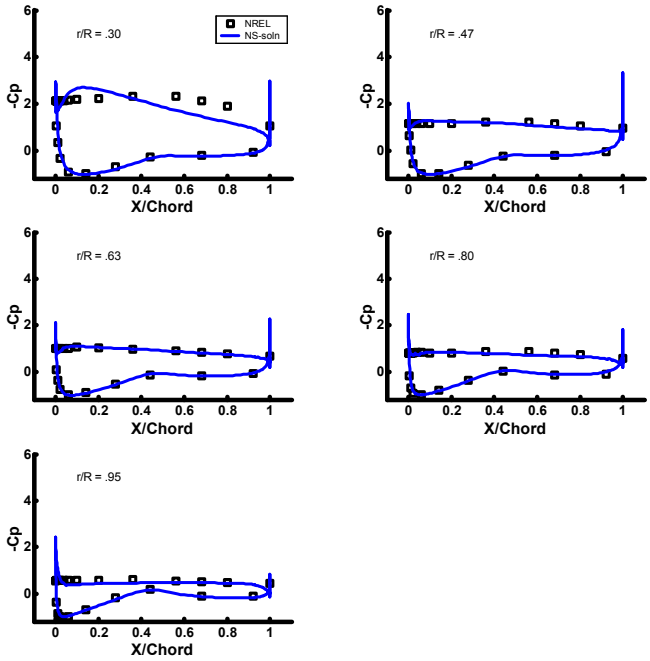


**Figure 10 - Pressure Coefficient, 20 m/s**

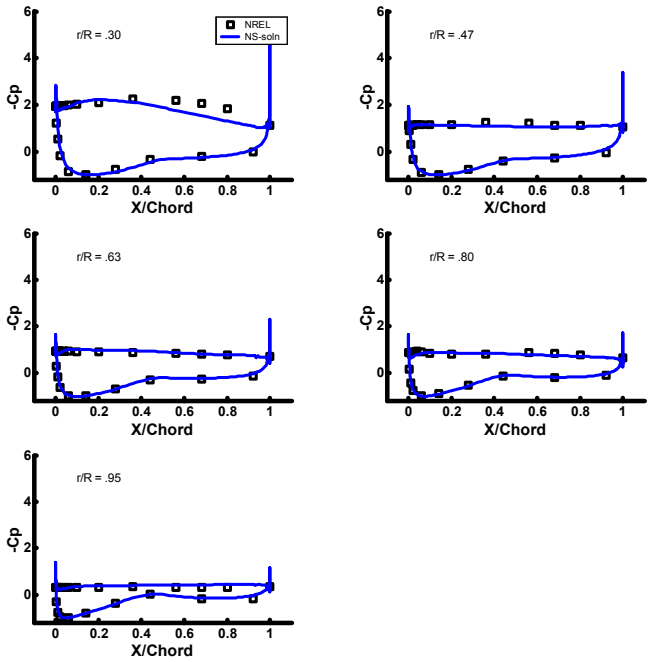


**Figure 11 - Pressure Coefficient, 25 m/s**

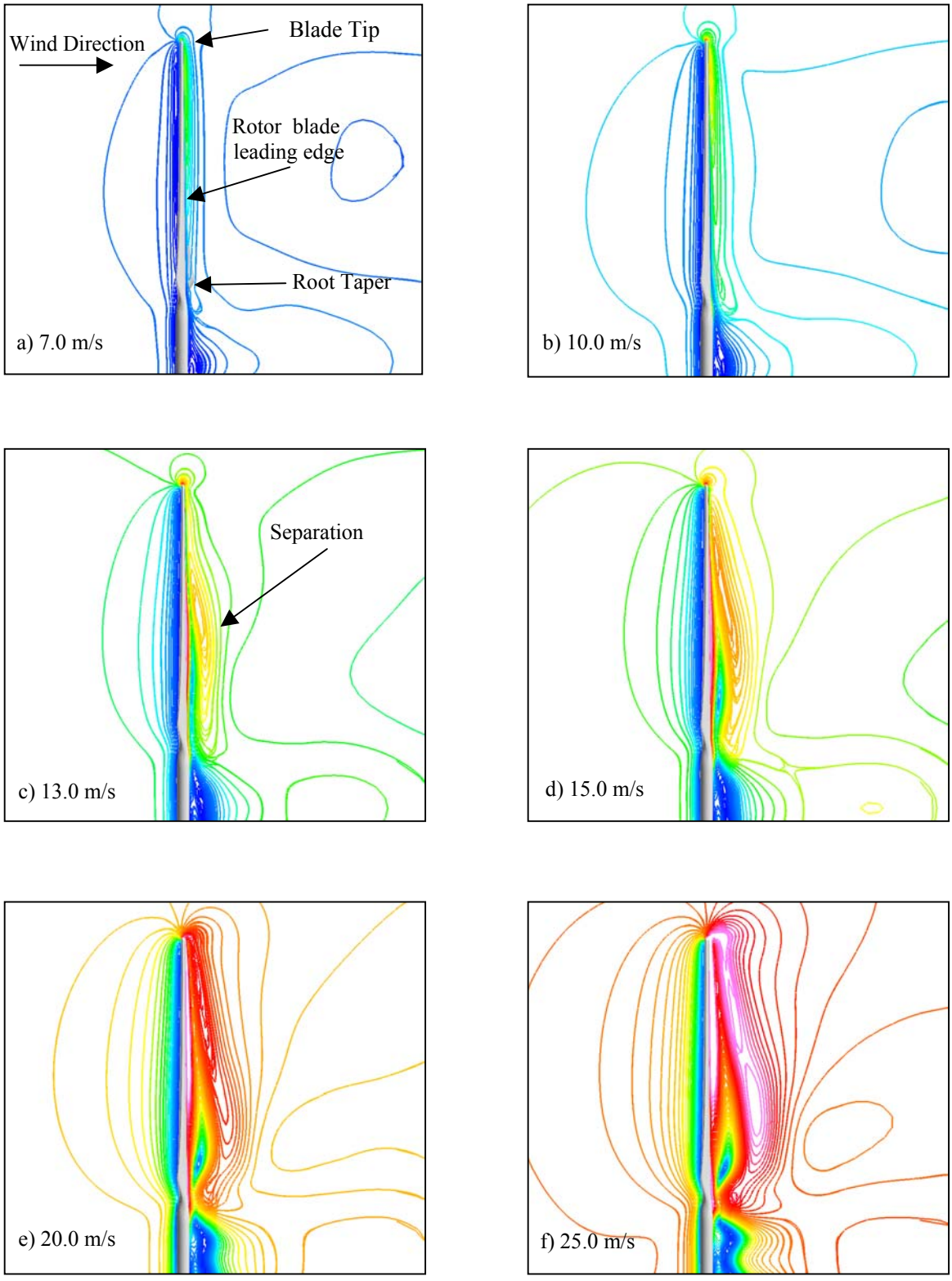


**Figure 12 - Velocity Contours Cut-Plane x=0.0**

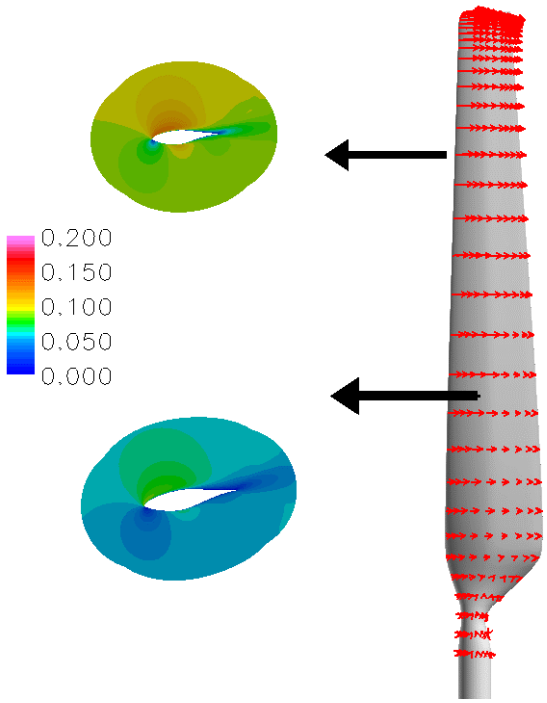


**Figure 13 - Velocity Contour and Vectors Non-Inertial Coordinates, 7 m/s**

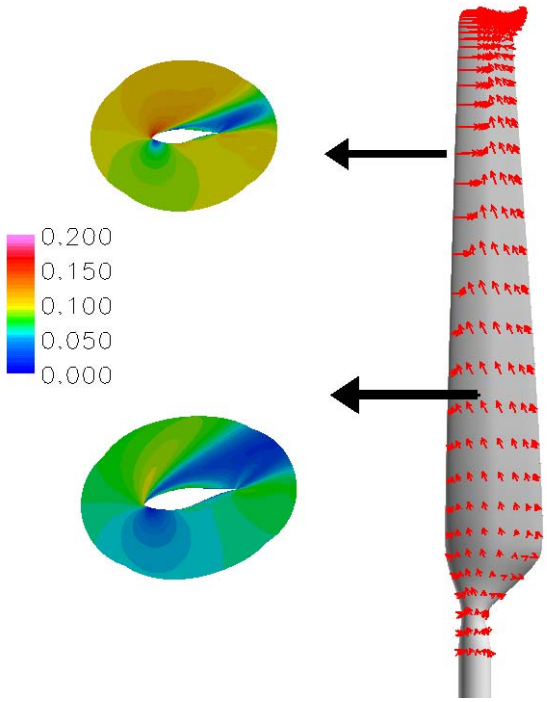


**Figure 14 - Velocity Contour and Vectors Non-Inertial Coordinates, 13 m/s**

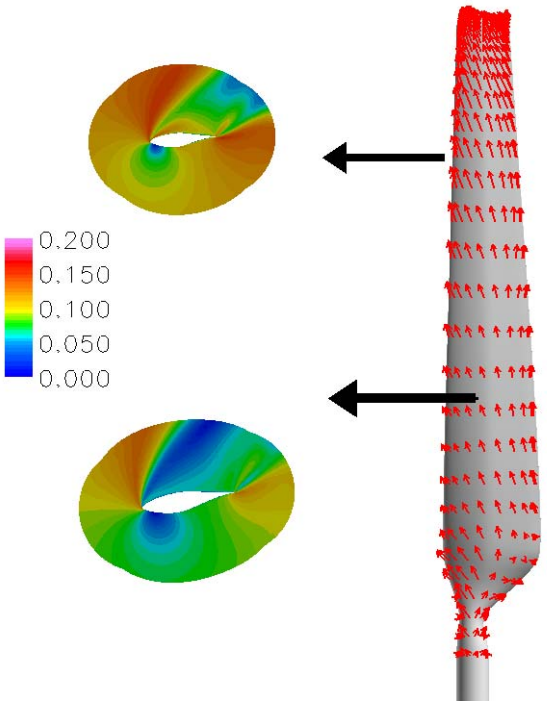


**Figure 15 - Velocity Contour and Vectors Non-Inertial Coordinates, 25 m/s**

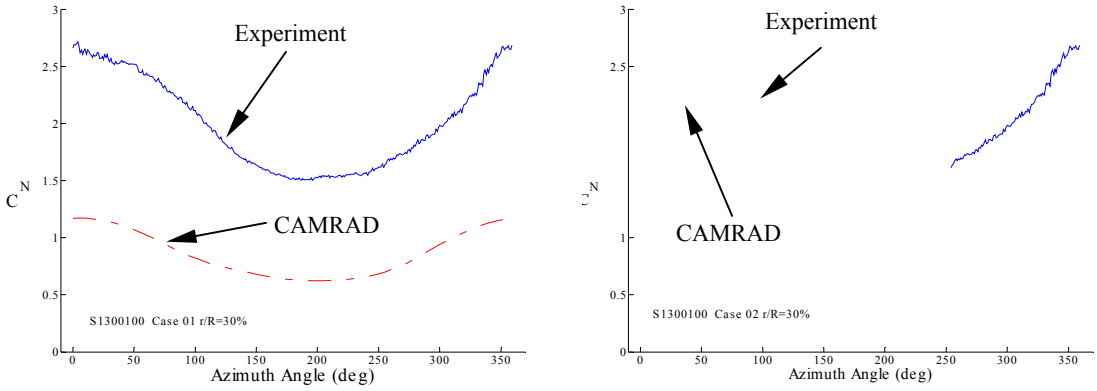


**Figure 16 - Effect of Stall Delay Model, 10 m/s, 10$^{O}$ Yaw Error, 30% span; without (case 01) and with (case 02) the stall delay model.**

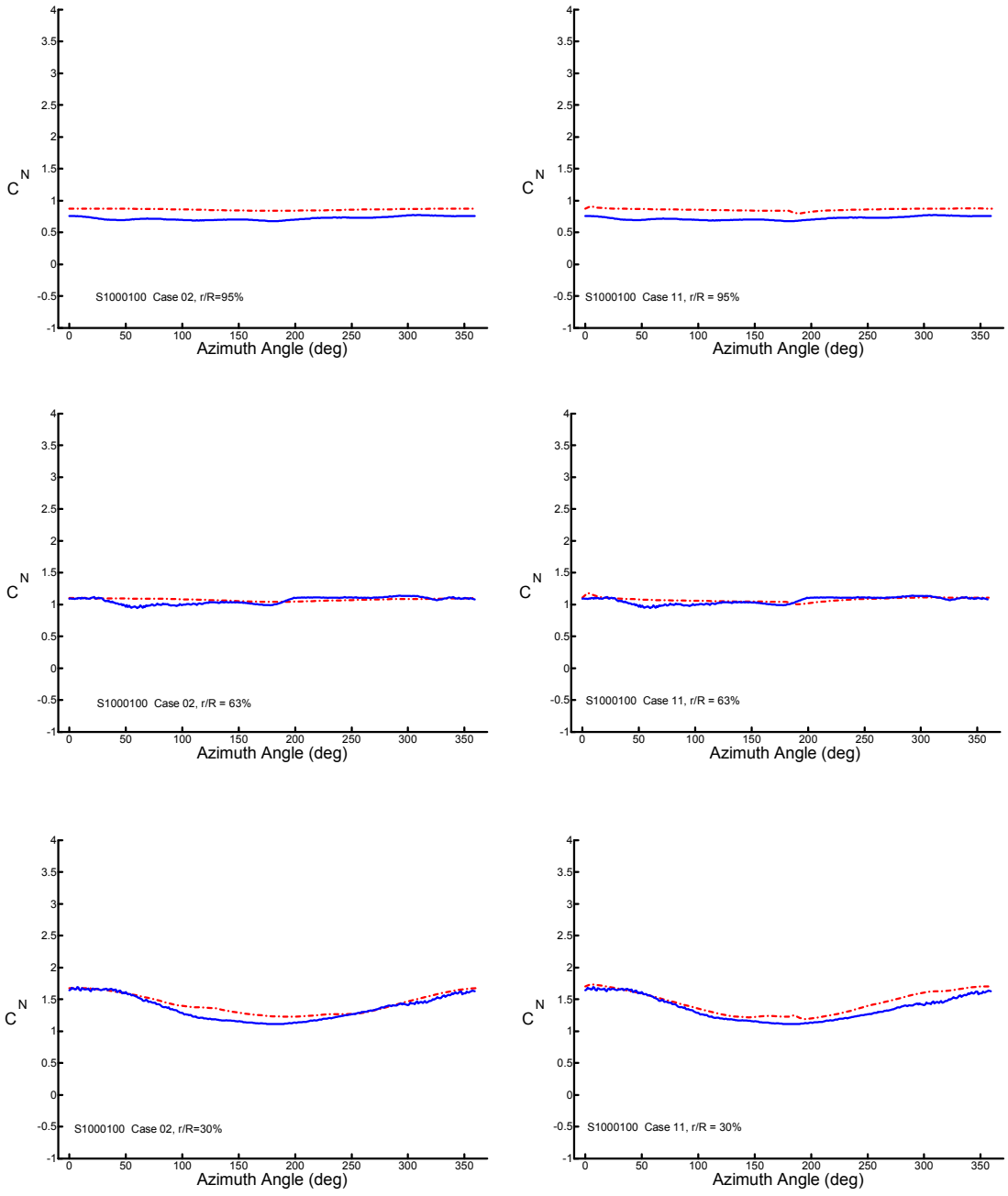


**Figure 17 - - Dynamic Stall Model Effect 10 m/s, $10^{O}$ Yaw Error**

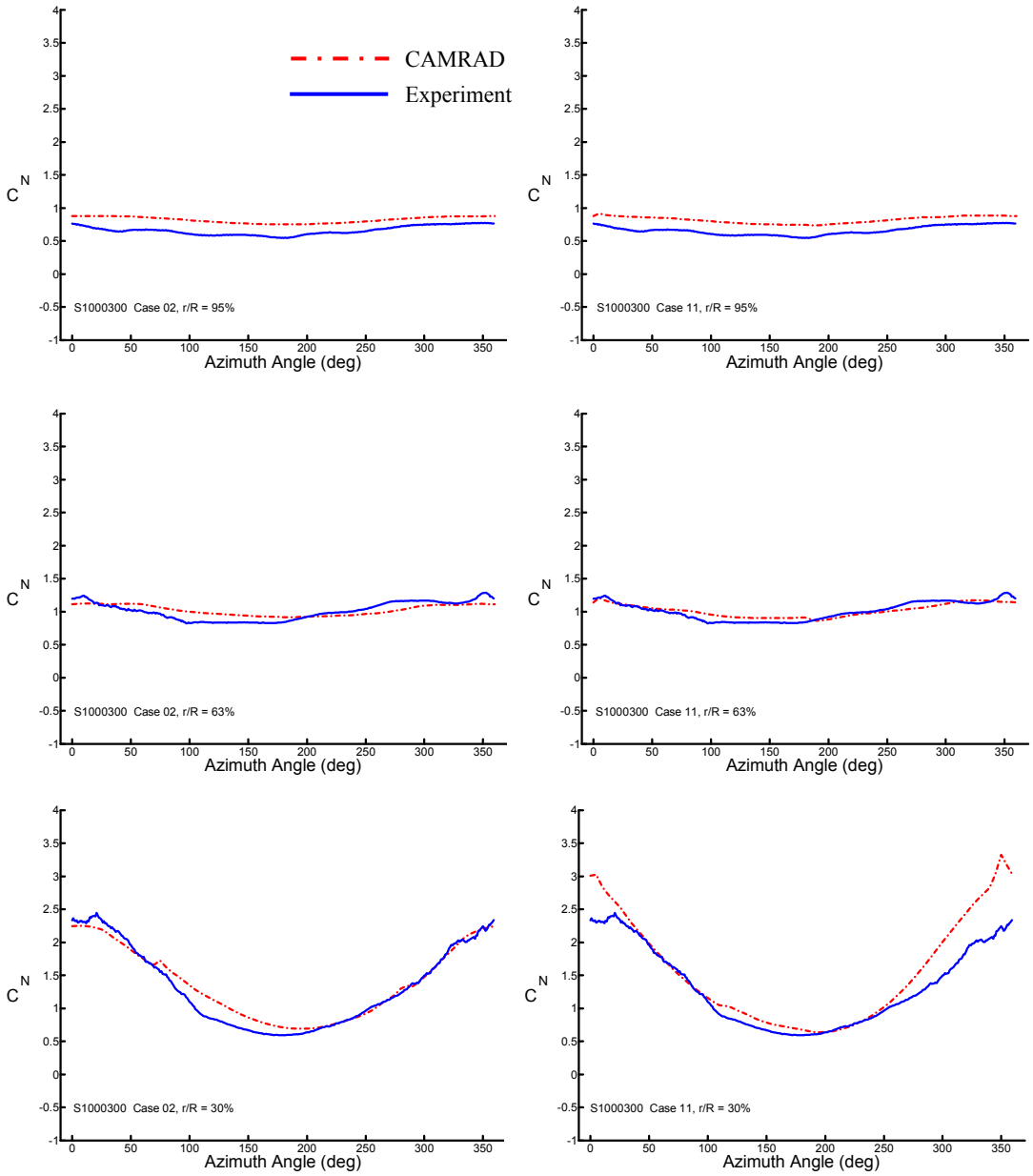


**Figure 18 - - Dynamic Stall Model Effect 10 m/s, 30$^{O}$ Yaw Error**

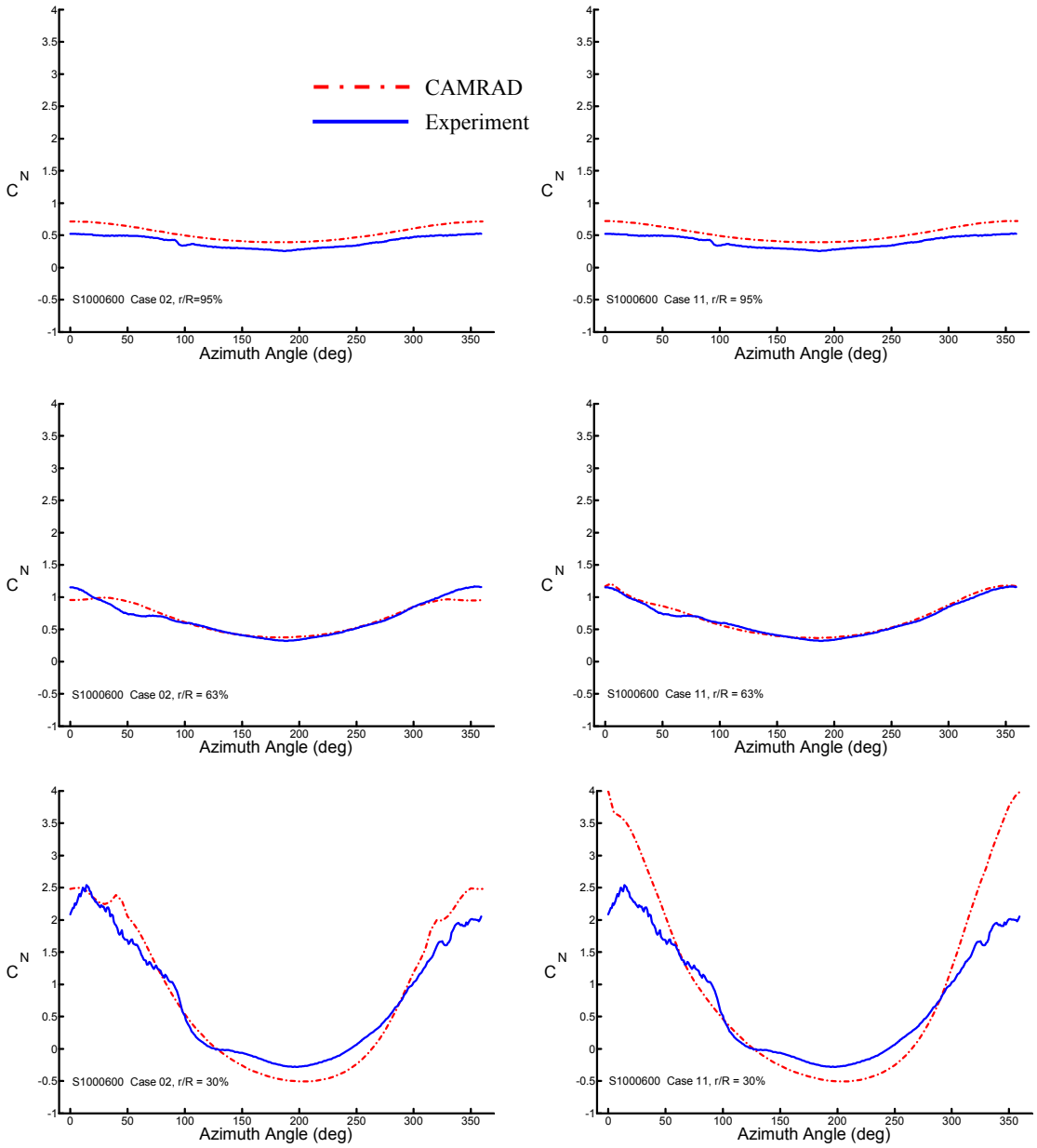


**Figure 19 - Dynamic Stall Model Effect 10 m/s, 60$^{O}$ Yaw Error**

## Reference

1. Rajagopalan, R.G., Fanucci, J.B., "Finite Difference Model for the Vertical Axis Wind Turbines", Journal of Propulsion and Power, Vol.1, pp.432-436, 1985.

2. Leclerc, C. and Masson, C, "Predictions of Aerodynamic Performance and Loads of HAWTS Operating in Unsteady Conditions", Proceedings 1999 ASME Wind Energy Symposium, 37th AIAA Aerospace Sciences Meeting and Exhibit, AIAA-99-0066, Reno, NV, January 1999

3. Whale, J., Fisichella, C.J., and Selig, M.S., Correcting Inflow Measurements from HAWTS using a Lifting Surface Code", Proceedings 1999 ASME Wind Energy Symposium, 37th AIAA Aerospace Sciences Meeting and Exhibit, AIAA-99- 0040, Reno, NV, January 1999

4. Sorenson, N.N., and Hansen, M.O.L, "Rotor Performance Predictions using a Navier-Stokes Method", Proceedings 1998 ASME Wind Energy Symposium, 36th AIAA Aerospace Sciences Meeting and Exhibit, AIAA-98-0025, Reno, NV, January 1998.

5. Xu, G., and Sankar, L., "Computational Study of Horizontal Axis Wind Turbines", Proceedings 1999 ASME Wind Energy Symposium, 37th AIAA Aerospace Sciences Meeting and Exhibit, AIAA-99-0042, Reno, NV, January 1999

6. Fingerish L., Simms D., Hand M., Jager D., Cortrell J., Robinson M., Schreck S. and Larwood S., " Wind Tunnel Testing of NREL's Unsteady Aerodynamics Experiment," 2001 ASME Wind Energy Symposium, pg 129-135, Reno, NV, January 2001, AIAA-2001-0035.

7. Schreck, Scott (Editor), Wind Energy, "Special Issue: Analysis and Modeling of the NREL Full-Scale Wind Tunnel Experiment", Volume 5, Number 2/3, April-September 2002.

8. Johnson, W., "Rotorcraft Aerodynamics Models for a Comprehensive Analysis," Presented at the American Helicopter Society Forum, Washington, D.C., May 1998.

9. Sommers, D.M., "Design and Experimental Results for the S809 Airfoil," NREL/SR-440-6918, January 1997. 12 Reuss Ramsay, R., Hoffman, M.J., and Gregorek, G.M., "Effects of Grit Roughness and Pitch Oscillation on the S809 Airfoil," NREL/TP-442-7817, 1995.

10. Drela, M., "Newton Solution of Coupled Viscous/Inviscid Multi-Element Airfoil Flows," AIAA Paper 90-1470, June 1990.

11. Drela, M.,"A User's Guide to MSES 2.95," MIT Computational Aerospace Sciences Laboratory, September 1996.

12. Snel, H. and van Holten, Th., "Review of Recent Aerodynamic Research on Wind Turbines with relevance to Rotorcraft, Data and riddles on Dynamic Inflow, Flowfield of Yawed Rotors and Rotating 3-D Stall", Proceeds of the Twentieth European Rotorcraft Forum, October 4-7, 1994.

13. Corrigan, J.J., and Schillings J.J., "Empirical Model for Stall Delay Due to Rotation", American Helicopter Society Aeromechanics Specialists Conference, San Francisco, CA, January 1994.

14. Du, Z., and Selig, M., "A 3-D Stall-Delay Model for Horizontal Axis Wind Turbine Performance Prediction", AIAA-98-0021, January 1998.

15. Buning, P., et.al., OVERFLOW Users Manual ver. 1.6ap.

16. Ahmad, J. and Duque, E.P.N., "Helicopter Rotor Blade Computation in Unsteady Flows Using Moving Overset Grids," Journal of Aircraft, Vol. 33, No. 1, Jan.-Feb. 1996, pp. 54-60.

17. Meakin, R., "Moving Grid Overset Grid methods for Complete Aircraft Tiltrotor Simulations," AIAA Paper 93-3350, July 1993.

18. Duque, E.P.N., vanDam, C.P. and Hughes, S., "Navier-Stokes Simulations of the NREL Combined Experiment Phase II Rotor", Proceedings 1999 ASME Wind Energy Symposium, 37th AIAA Aerospace Sciences Meeting and Exhibit, AIAA-99-0037, Reno, NV, January 1999.

19. Chan, W.M , Meakin, R. and Potsdam, M., "CHSSI Software for Geometrically Complex Unsteady Aerodynamic Applications," AIAA 01-0593, Jan 8 2001, Reno NV

20. Chan, W.M., ".The OVERGRID Interface for Computational Simulations on OVERSET Grids", 32nd AIAA Fluid Dynamics Conference, St.Louis Missouri, AIAA-2002-3188, June 2002.

21. Baldwin, B.S., and Lomax, H., " Thin-Layer Approximation and Algebraic Model for Separated Turbulent Flow, "AIAA Paper 78-0257, Jan 1978.

22. Baldwin, B.S. and Barth, T.J., "A One-Equation Turbulence Transport Model for High Reynolds Number Wall-Bounded Flows," NASA TM 102847, Aug. 1990

23. www.redhat.com, Redhat version 7.1 is a version of the Linux Operating system.